*remote sensing*

MDPI

*Article*

# Cloud Type and Life Stage Dependency of Liquid–Ice Mass Partitioning in Mixed-Phase Clouds

**Jing Yang [1,2,*], Yue Zhang [1], Zhien Wang [3,4] and Damao Zhang [5]**

[1] Key Laboratory for Aerosol Cloud-Precipitation of China Meteorological Administration, Key Laboratory of Meteorological Disaster, Ministry of Education (KLME), Joint International Research Laboratory of Climate and Environment Change (ILCEC), Collaborative Innovation Center on Forecast and Evaluation of Meteorological Disasters (CIC-FEMD), Nanjing University of Information Science & Technology, Nanjing 210044, China; 20211203036@nuist.edu.cn
[2] Shanghai Typhoon Institute, China Meteorological Administration, Shanghai 200032, China
[3] Department of Atmospheric and Oceanic Sciences, University of Colorado, Boulder, CO 80309, USA; zhien.wang@colorado.edu
[4] Laboratory for Atmospheric and Space Physics, University of Colorado, Boulder, CO 80303, USA
[5] Atmospheric Sciences and Global Change Division, Pacific Northwest National Laboratory, Richland, WA 99354, USA; damao.zhang@pnnl.gov
* Correspondence: jing.yang@nuist.edu.cn

**Abstract:** This paper analyzes the temperature, cloud type, and life stage dependencies of phase partitioning in mixed-phase clouds spanning tropics, midlatitudes, and the Arctic, using data from ground-based remote sensing measurements in Alaska and aircraft measurements from three field campaigns. The results show: (1) The liquid fraction in Arctic stratiform clouds decreased from 1 to 0.6 between 0 °C and −30 °C and was lower in spring because of the higher dust occurrence in Barrow, Alaska; (2) In wintertime orographic clouds, the liquid fraction was greater than 0.8; (3) Phase partitioning in convective clouds varied significantly with life stages. In the developing stage, it decreased from 1 to 0.3 between −5 °C and −15 °C, indicating rapid ice generation, while at the mature and dissipating stages, the liquid fractions were lower; (4) The stratiform regions of mesoscale convective systems were dominated by ice, with liquid fractions lower than 0.2; and (5) The variability of phase partitioning varied for different cloud types. In stratiform clouds, liquid dominated at warm temperatures. As the temperature decreased, an ice-dominated region was more frequently observed, while the occurrence of the mixed-phase region remained low. For convective clouds, the variability of phase partitioning was controlled by continuous glaciation with decreasing temperature and life cycle.

**Keywords:** mixed-phase clouds; liquid–ice mass partitioning; ground-based remote sensing; airborne measurement



**Citation:** Yang, J.; Zhang, Y.; Wang, Z.; Zhang, D. Cloud Type and Life Stage Dependency of Liquid–Ice Mass Partitioning in Mixed-Phase Clouds. *Remote Sens.* **2022**, *14*, 1431. https://doi.org/10.3390/rs14061431

Academic Editor: Maria João Costa

Received: 1 February 2022
Accepted: 13 March 2022
Published: 16 March 2022



## 1. Introduction

Mixed-phase clouds are important for the global radiation budget and water cycle [1], but phase (liquid or ice) partitioning in mixed-phase clouds is still not well understood [2]. Representations of microphysics in mixed-phase clouds have been regarded as important sources of uncertainties in models [1,3]. The complicated ice physics and the interactions between liquid water and ice make modeling phase partitioning in mixed-phase clouds challenging [3,4]. In addition, different cloud types (stratiform and convective) have different phase partitioning properties. Understanding phase partitioning in different types of mixed-phase clouds is critical to improving general circulation models (GCMs) and numerical weather prediction models (NWPMs).

Stratiform mixed-phase clouds are the dominant cloud type at high latitudes and have a large global coverage [2,4]. GCMs have large uncertainties in modeling phase partitioning in mixed-phase stratiform clouds because of their low resolution and poorly parameterized

ice nucleation [5,6] and liquid–ice interactions [7]. Observations are needed to improve model simulations of mixed-phase clouds. Airborne in situ measurements have been useful tools in studying the microphysics in stratiform mixed-phase clouds, as they can accurately measure the microphysical properties, such as particle size distributions (PSD) [8], but the sample volume of an aircraft penetration is small and a research flight is typically limited to 4 h.

Long-term remote sensing measurements, such as those using millimeter cloud radar, lidar, and microwave radiometer, can provide much larger datasets to study macro- and microphysics in stratiform mixed-phase clouds [9–11]. For example, previous studies investigated phase partitioning in Arctic stratiform mixed-phase clouds using ground-based remote sensing measurements at the North Slope of Alaska (NSA) site operated by the Department of Energy's Atmospheric Radiation Measurement (ARM) Program [10,12,13]. Retrieved microphysical variables have been used to evaluate model simulations [2,4], and algorithms developed based on ground-based or airborne-based remote sensing observations have been applied to satellite measurements, which provide global distributions of stratiform mixed-phase cloud microphysical properties [14].

Convective clouds have very different dynamic and microphysical properties than stratiform clouds [15–17]. GCMs have large uncertainties when modeling the dynamics and microphysics of convective clouds, due to their low resolutions and unresolved physical processes [18]. Cloud-resolving models (CRM) with higher resolutions can better resolve microphysical processes, but difficulties inherent in parameterizing microphysics remain a main source of uncertainties in CRM simulations [3]. Remote sensing is not the best tool to quantitatively study the microphysics of convective clouds, because convective clouds are usually optically thick, and their hydrometeor habits (e.g., large drops, graupel and ice aggregates) are more complicated than the habits of stratiform clouds, resulting in large uncertainties in the retrieved microphysical properties [19]. Airborne in situ measurements have been widely used to study the microphysics of convective clouds [15,20–22]. Because sample sizes of airborne in situ measurements are relatively small, and for safety concerns, aircraft (except storm penetrating aircraft) measurements often have to keep away from convective cores, especially in mesoscale convective systems (MCSs) [23]. In addition, instruments mounted on aircraft have limitations; for example, in distinguishing large drops from ice particles, detecting small ice particles, and measuring total water content (TWC) [17]. Therefore, more airborne in situ measurements, with more advanced instruments, are needed to better understand phase partitioning in convective clouds.

Though the differences in dynamics and microphysics in stratiform and convective clouds have been recognized in previous studies, liquid-ice mass partitioning in different types of clouds has not been well compared quantitatively, and is still poorly parametrized [6,24–26]. In addition, the differences in the variability of phase partitioning in different cloud types are not well understood. Therefore, the present study aims to qualitatively analyze the liquid–ice mass partitioning in stratiform and convective mixed-phase clouds, focusing on temperature, cloud type, and life stage dependencies. The variability of phase partitioning and the differences among different cloud types are also discussed.

The data were collected from six years of ground-based remote sensing measurements at the NSA site for Arctic stratiform mixed-phase clouds, airborne in situ measurements from the Ice in Clouds Experiment-Layer Clouds (ICE-L) project for orographic mixed-phase clouds, the Ice in Clouds Experiment-Tropical (ICE-T) project for tropical maritime convective clouds, and the Midlatitude Continental Convective Clouds Experiment (MC3E) project for continental MCSs. We also used the in-situ measurements from the Mixed-Phase Arctic Cloud Experiment (M-PACE) as an aid in investigating the vertical structure of liquid–ice mass partitioning in Arctic stratiform mixed-phase clouds. Analysis methods for different datasets have been fully evaluated and applied in previous studies [9,17,23,27–31].

This paper is organized as follows: Section 2 introduces the datasets and the analysis methods; Section 3 shows the results; a discussion is provided in Section 4; and the conclusions are presented in Section 5.

## 2. Datasets and Analysis Method

In this section, the datasets and analysis method are described, including the microphysical variables retrieved using ground-based remote sensing techniques, and those measured using airborne in situ observations. Since all the retrieval and processing methods have been detailed in previous papers, and the datasets are publicly available (the links of the datasets are shown in Data Availability Statement), we only briefly describe the derivation of the microphysical variables that are used in the present paper, together with their uncertainties.

### *2.1. Ground-Based Remote Sensing and Aircraft Measurements at NSA Site*

The NSA's Barrow site (71°19′ N, 156°36′ W), which is operated by the ARM program, has been used to sample Arctic stratiform clouds since 1997. In this study, we use data collected from 1999 to 2004 by a microwave radiometer (MWR), 35-GHz millimeter cloud radar (MMCR), and a micropulse lidar (MPL) to explore phase partitioning in single-layer Arctic stratiform mixed-phase clouds; multi-layer clouds were excluded in the analysis. The instruments and the measured and retrieved quantities are listed in Table 1.

**Table 1.** Description of datasets, instruments, and measured and derived quantities.

| Datasets | Cloud Type | Instruments | Properties | Measured and Derived Quantities |
|---|---|---|---|---|
| NSA 2009–2014 | Arctic stratiform clouds | MMCR | 34.86 GH, 45-m vertical resolution, 10-s temporal resolution | Reflectivity factor, cloud top height, IWC |
| | | MPL | 523 nm wavelength, 30-m vertical resolution, 30-s temporal resolution | Cloud extinction, cloud base height, cloud top height for optically thin clouds, IWC |
| | | MWR | 23.8 GHz and 31.4 GHz, column integrated, 30-s temporal resolution | Brightness temperature, LWP |
| M-PACE 2004.10.9–2004.10.12 | Arctic stratiform clouds | King probe | LWC range: 0.05–3.0 g $m^{-3}$ | LWC |
| | | FSSP | Particle size range: 1–50 μm | PSD, LWC if King probe is not available |
| | | 2D-C | Particle size range: 25–3200 μm (the first 3 bins were not used) | PSD, particle images, IWC |
| | | HVPS | Particle size range: 300–30,000 μm | PSD, particle images, IWC |
| ICE-L 2007.11.7–2007.12.16 | Midlatitude orographic clouds | King probe | LWC range: 0.05–3.0 g $m^{-3}$ | LWC |
| | | 2D-C | Particle size range: 25–3200 μm (the first 3 bins were not used) | PSD, cloud particle images, IW |
| | | 2D-P | Particle size range: 200–12,800 μm | PSD, precipitation particle images, IWC |
| ICE-T 2011.7.1, 2011.7.22–2011.7.30 | Tropical maritime convective clouds | King probe | LWC range: 0.05–3.0 g $m^{-3}$ | LWC carried by droplets |
| | | Fast 2D-C | Particle size range: 25–3200 μm | PSD, LWC carried by drops, cloud particle images, IWC |
| | | Fast 2D-P | Particle size range: 150–19,200 μm | PSD, precipitation particle images, IWC |
| | | CVI | TWC range: 0.01–2.5 g $m^{-3}$ | TWC |
| MC3E 2011.4.22–2011.6.2 | Midlatitude mesoscale convective systems | King probe | LWC range: 0.05–3.0 g $m^{-3}$ | LWC |
| | | 2D-C | Particle size range: 25–3200 μm (the first three bins were not used) | PSD, cloud particle images, IWC |
| | | HVPS | Particle size range: 300–30,000 μm | PSD, precipitation particle images, IWC |

The cloud base was determined from an MPL measurement on the basis that the MPL extinction coefficient (σ) obtained a rapid change near the cloud boundaries. The cloud top was estimated by both MPL σ and radar Ze, and the higher one is used. For most of the clouds, the top determined using radar Ze is higher, while for some optically thin clouds, the top determined using lidar was higher. The Liquid Water Path (LWP) was retrieved based on two-channel MWR measurements (Table 1) using the algorithm developed by Wang [31]. The accuracy of the brightness temperature measurements was approximately 0.3 K, and the resolution was 0.25 K. This retrieval algorithm has an uncertainty of approximately 0.3 g $m^{-2}$ for clear sky LWP, and the standard deviation was 4 g $m^{-2}$ [31]. The ice phase properties of the NSA clouds, including the ice water content (IWC) and general equivalent diameter (Dge), were retrieved based on MMCR Ze and MPL σ using the algorithm developed by Wang and Sassen [9,27]. The Ze–IWC and Ze–Dge statistical relationships were determined using the retrieved IWC and Dge below the cloud bases and then applied to the mixed-phase layers. This algorithm was originally developed for cirrus clouds, but has been successfully applied to liquid-topped mixed-phase stratiform clouds. The main uncertainties of the IWC came from the assumptions of PSD and ice shape in the retrieval, which resulted in an uncertainty of approximately 9% in the retrieved IWC in mixed-phase stratiform clouds [30]. The ice water path (IWP) was calculated by integrating the IWC from the cloud bases to the tops. The liquid fraction, which is widely used to describe phase partitioning, is defined as the ratio of the LWP to the total water path (TWP = LWP + IWP). The cloud top temperatures (CTTs) were estimated using the merged sounding data, which used a combination of radiosonde observations, MWR, surface meteorological observations, and European Centre for Medium Range Weather Forecasts (ECMWF) model outputs [32]. In 2008 at Barrow, Alaska, Protate et al. [33] found a calibration offset of 9.8 dB for the MMCR measurement, but this was not found for the data (1999–2004) used in this study.

Long-term ground-based remote sensing measurements are useful in investigating the seasonal differences in liquid–ice mass partitioning in Arctic mixed-phase clouds. In order to investigate the vertical structure of phase partitioning in the mixed-phase region of single-layer Arctic stratiform clouds, we also used the aircraft in situ measurements during M-PACE. M-PACE was conducted in October 2004, where the University of North Dakota (UND) Citation aircraft [28] was deployed to make spiral penetrations in Arctic stratiform clouds. The measurements of microphysical properties were processed using the algorithm described in [28], and the data was archived on the ARM data archive (http://www.archive.arm.gov/) (accessed on 25 January 2022). The LWC was measured using a King probe [34] if available; otherwise, it was estimated using the particle size distributions (PSDs) from a Forward Scattering Spectrometer Probe (FSSP). The *IWC* was estimated using the mass-size relation based on PSDs from a two-dimensional cloud (2D–C) imaging probe and a High-Volume Precipitation Spectrometer (HVPS):

$$IWC = \sum_{D_{min}}^{D_{max}} aD^b N(D) \quad (1)$$

where $D$ is the particle diameter in μm, which is defined as the maximum length of a particle image; the values of a and b are listed in Table 2 [33]. The liquid fraction is defined as the ratio of the LWC to the TWC (TWC = LWC + IWC). Only measurements with LWCs exceeding 0.05 g $m^{-3}$ were used; thus, ice clouds (region) were not included. In this study, we used research flights conducted on 9, 10 and 12 October 2004. These research flights were made in the same cloud system, and the sampling duration made in this cloud system was much longer than for others. In addition, spiral penetrations were made from cloud top to cloud base; therefore, these research flights provided good measurements of the vertical structure of liquid–ice mass partitioning in these Arctic mixed-phase stratiform clouds. The results could be used to evaluate the ground-based retrievals.

**Table 2.** The values of a and b in Equation (1) for different experiments.

| Project | A | B |
|---|---|---|
| M-PACE | $1.07 \times 10^{-10}$ | 1.7 |
| ICE-L | $4.82 \times 10^{-11}$ | 1.9 |
| MC3E | $1.45 \times 10^{-11}$ | 2.1 |

### *2.2. Aircraft In Situ Measurements for ICE-L, ICE-T, and MC3E*

The ICE-L project was conducted from November through December 2007 in the mountainous western United States. Aircraft of The National Center for Atmospheric Research (NCAR) C-130 were deployed to penetrate orographic mixed-phase clouds (mostly stratiform) at true air speeds of approximately 150 m $s^{-1}$. There were 12 research flights in total. In this study, the LWC measured using a King probe and the IWC estimated using the PSDs measured by two-dimensional (2D) imaging probes were used to investigate the phase partitioning in ICE-L clouds (Table 1). The IWC was estimated based on the mass-size relation developed by Locatelli and Hobbs [35] and Hogan et al. [36] (Equation (1) and Table 2). This relation was originally developed for unrimed ice aggregates; it has been widely used for cirrus and stratiform clouds [36,37] and is recommended for ICE-L clouds [29]. The liquid fraction is defined as the ratio of the LWC to the TWC. Only measurements with LWCs exceeding 0.05 g $m^{-3}$ were used; thus, pure ice clouds (regions) were not included. All the measurements were averaged to 1 s, indicating a spatial resolution of approximately 150 m.

The ICE-T project was conducted from 1 July to 30 July 2011 over the Caribbean Sea, with the aim of studying ice generation in tropical maritime convective clouds. The NCAR C-130 was among the primary research aircraft deployed in ICE-T. The temperatures were measured using a Rosemount sensor. The LWC was measured from the King probe, and the drops identified from particle images were recorded by a fast 2D-C and a fast 2D-P probe. The drop identification approach was developed by Yang et al. [17], based on particle images using the Fourier transform technique and the aspect ratio of the particles. The TWC was measured by a counterflow virtual impactor (CVI) probe [38], and the IWC was calculated from the TWC minus the LWC. If the LWC exceeded the TWC measured by the CVI, the TWC was assumed to be equal to the LWC. Measurements with LWCs exceeding 0.05 g $m^{-3}$ were used to study the phase partitioning; thus, pure ice clouds (regions) were not included. All data were averaged to 1 s. In this study, we used seven research flights in which Wyoming Cloud Radar (WCR), a 95-GHz-pulsed Doppler radar that was on board, was operating. We classified the convective clouds sampled in ICE-T into three stages, based on WCR Ze and flight-level vertical velocity, as follows: (1) Developing clouds, which are defined as updraft cores nearly reaching ($\leq$500 m) the cloud tops; (2) Mature clouds, which are defined as updraft cores far below (>500 m) the cloud tops; and (3) Dissipating clouds/dissipating parts of mature clouds, in which no updraft core was observed and the flight level was far below (>500 m) the cloud tops. This classification followed Yang et al. [17]. An updraft core is defined as an ascending parcel with a vertical velocity of no less than 1 m $s^{-1}$ and a diameter of at least 500 m [39].

The MC3E project was conducted from April to June 2011 in the southern Great Plains of the United States. UND Citation II aircraft [23] were among the primary research aircraft deployed during MC3E. Fifteen research flights were made during the project. Due to safety concerns, the aircraft in situ measurements were primarily made in the stratiform parts of the MCSs. The temperature was measured using a Rosemount sensor. The LWC was measured using a King probe, and large drops were rarely found in the stratiform parts of the MCSs. Ice PSDs were measured using a 2D-C and HVPS (Table 1). The IWC was estimated using a mass-size relation developed specifically for MC3E measurements [23] (Equation (1) and Table 2). The measurements with LWCs exceeding 0.05 g $m^{-3}$ were used to study the phase partitioning in MC3E clouds. Liquid fraction is defined as the ratio of the LWC to the TWC. The data were averaged to 1 s, i.e., the spatial resolution was approximately 100 m.

The uncertainties of liquid fraction measured by aircraft were determined by both the LWC and the IWC. The King probe reliably measured the LWC > 0.05 g $m^{-3}$ carried by droplets, with a random error of 15%. For LWC < 0.05 g $m^{-3}$, the noise and drift effects from changing airspeed impact the LWC signal. For drops larger than 50 μm in diameter, the King probe underestimates the LWC. In ICE-L, M-PACE and MC3E, few large drops were observed, while in ICE-T, the LWC carried by large drops was derived using the PSDs of drops identified from the 2D-C and 2D-P measurement. Because the quasi-spherical ice particles (e.g., frozen drops) may be identified as liquid drops, the calculated LWC in ICE-T was overestimated by 10% when the LWC exceeded 1 g $m^{-3}$ [17]. This uncertainty was obtained by comparing the derived LWC to the TWC measured by the CVI in a pure liquid region and were sometimes lower because deformed liquid drops are regarded as ice (i.e., compensating error) [17]. The IWC was derived from the TWC minus the LWC in ICE-T, so the uncertainty of the IWC was determined by the CVI TWC and the derived LWC. The CVI reliably measured the TWC from 0.01 g $m^{-3}$ to 2.5 g $m^{-3}$, with a random error of 20% [38]. TWCs greater than 2.5 g $m^{-3}$ were rarely found in the data used in this study [17]. In addition, the CVI had a cut size of 8 μm in diameter, but the TWC in ICE-T clouds was mainly contained in particles larger than 8 μm in diameter [17]. For ICE-L, MC3E, and M-PACE, the IWC was derived using the mass-size relation of ice, which definitely caused uncertainties. The coefficients of the mass-size relation (Table 2) provided the best estimates of the IWC for these datasets. For example, for MC3E, the coefficients were determined by comparing the derived IWC against the IWC measured by the Nevzorov probe in pure ice regions. For M-PACE, the coefficients were determined by comparing the derived IWC against the IWC measured by the CVI in ice-phase clouds.

It is worth noting that the definitions of liquid fraction using ground-based remote sensing (LWP/TWP) and aircraft measurements (LWC/TWC) are different. The liquid fraction derived using LWP/TWP is actually the vertically integrated LWC divided by the TWC, which is the same as the vertically averaged LWC divided by the TWC. Given that aircraft penetrations were made at multiple levels in ICE-L, ICE-T, and MC3E, it is reasonable to statistically compare the liquid fractions derived using ground-based remote sensing and aircraft measurements. In order to confirm this, the aircraft measurements from M-PACE were used to evaluate the liquid fraction retrieved using ground-based remote sensing, and the results suggested that the liquid fractions derived using different techniques have similar magnitudes (see the details in Section 3.2). In addition, in the following analysis, the CTTs were used for the Arctic clouds that were investigated using ground-based remote sensing, while flight-level temperature was used for the aircraft measurements. If the temperatures inside clouds were used instead of the CTTs, the retrieved liquid fraction would have had a different temperature dependency, but this impact was not significant, given that most of the Arctic stratiform clouds were shallow and the difference in the liquid fraction among the different cloud types were large (see the details in Section 3.2). This can again be confirmed by comparing the retrieved liquid fraction with the in-situ liquid fraction measured during M-PACE.

## 3. Results

### *3.1. Characteristics of the Observed Clouds*

In this section, examples of the observed clouds are provided, and their characteristics are delineated (Figures 1 and 2). An example of NSA clouds sampled on October 10, 2004, is shown in Figure 1 and includes MMCR Ze, MPL σ, retrieved IWC, liquid fraction, LWP, and IWP calculated by integrating the IWC from cloud bases to tops. The cloud base and top are shown by the black and red lines in Panel a-c. It is seen that the depth of this cloud was shallow (~600 m) and the cloud top varied between 1 km and 1.6 km (Figure 1a). The MMCR Ze had large variations, with a maximum Ze of approximately 15 dBZ. The retrieved IWC was relatively high near the cloud base, with typical values of 40–80 mg $m^{-3}$ in the areas where Ze > 10 dBZ, decreasing towards the cloud tops and the ground (Figure 1c). The MPL σ effectively separated the cloud layer and the snow layer, but the signal rapidly

attenuated due to the high concentration of liquid droplets (Figure 1b). The LWP (Figure 1f) was approximately 5–10 times larger than the IWP (Figure 1e), resulting in the liquid fraction mostly higher than 0.8 (Figure 1d). Relatively small liquid fraction was seen where the IWP was greater than 30 g $m^{-2}$, corresponding to a relatively high cloud top during the day (e.g., 2:00–4:00 UTC and after 15:00 UTC). The vertical velocity and the TWC observed in Arctic stratiform clouds during M-PACE are shown in Figure 3a,e. The vertical velocity was mostly weaker than 2 m $s^{-1}$, and similar magnitudes were observed for both the updrafts and downdrafts. The weak updrafts and the shallow cloud depth resulted in a low TWC, which was mostly lower than 0.5 g $m^{-3}$.

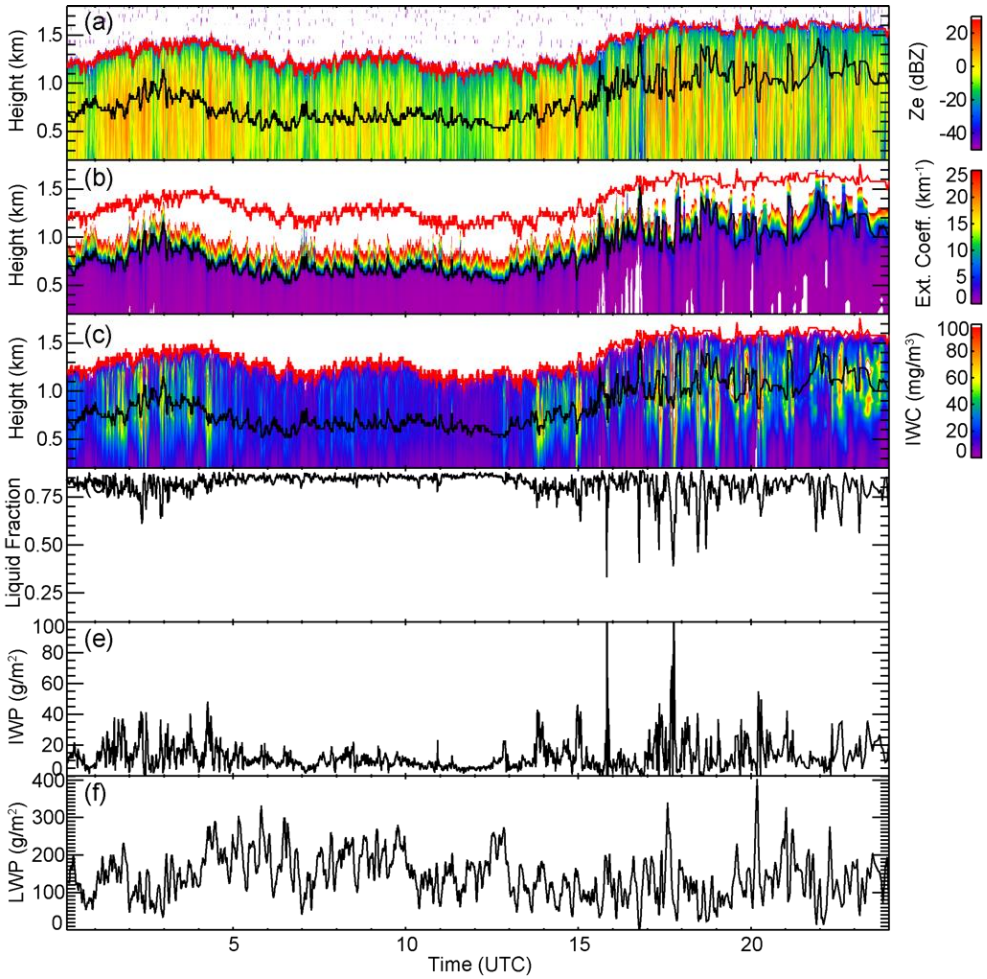


**Figure 1.** Examples of Arctic stratiform mixed-phase clouds sampled over the NSA site on October 10, 2004, including (**a**) MMCR Ze, (**b**) MPL extinction coefficient, (**c**) retrieved IWC, (**d**) liquid fraction, (**e**) IWP, and (**f**) LWP. The black and red lines in (a-c) represent the cloud base and the cloud top.

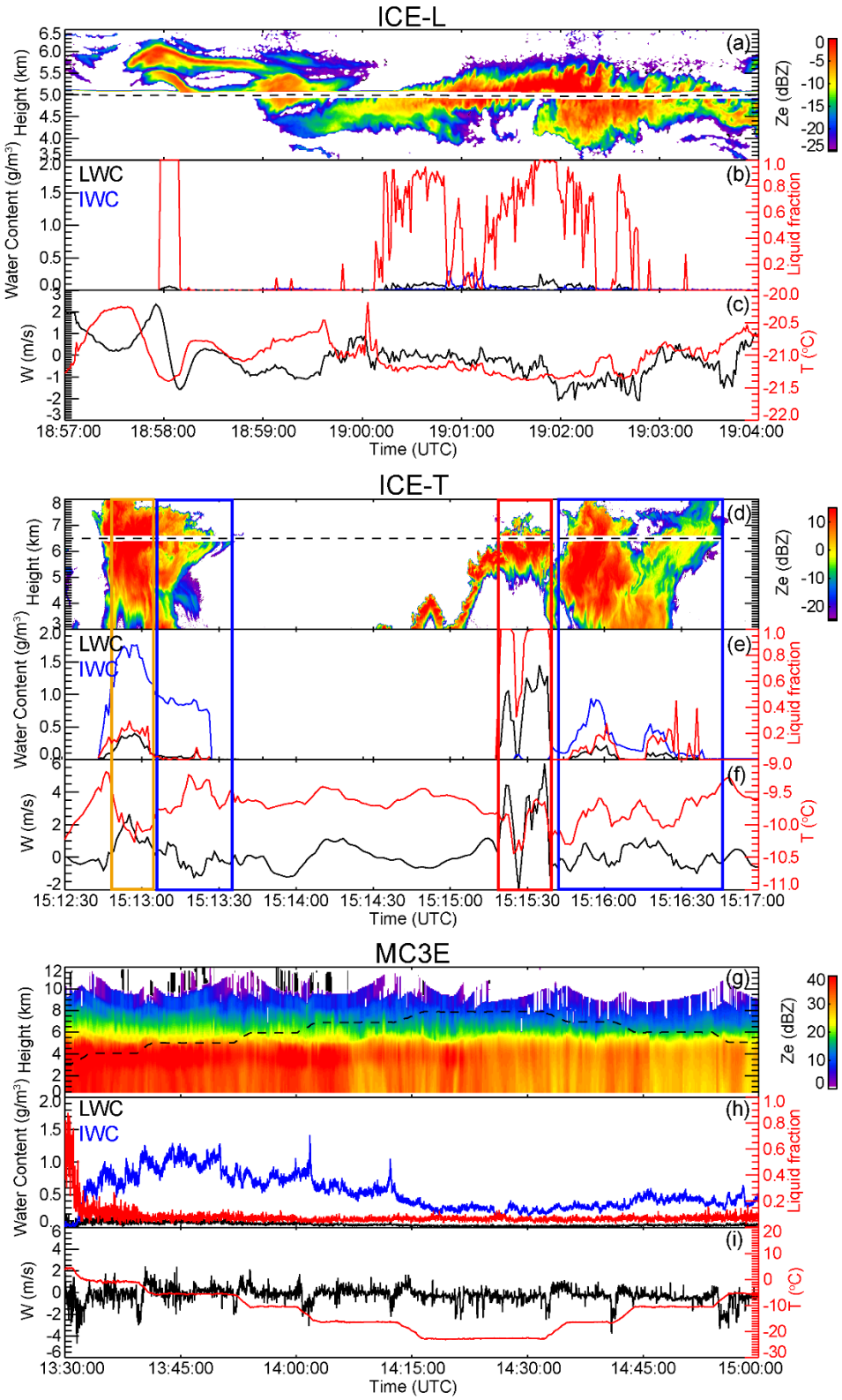


**Figure 2.** Examples of clouds sampled during ICE-L, ICE-T, and MC3E, including radar Ze (**a**,**d**,**g**), flight-level LWC, IWC, and liquid fraction (**b**,**e**,**h**), and vertical velocity and temperature (**c**,**f**,**i**). The Ze in (**a**,**d**) were measured by WCR in ICE-L and ICE-T, and Ze in (**g**) was measured using the WSR-88D scanning radar. The dashed lines in (**a**,**d**,**g**) indicate the flight levels. The red, orange, and blue boxes in (**d**–**f**) indicate the developing cloud, the mature cloud, and the dissipating cloud/ dissipating part of a mature cloud, respectively.

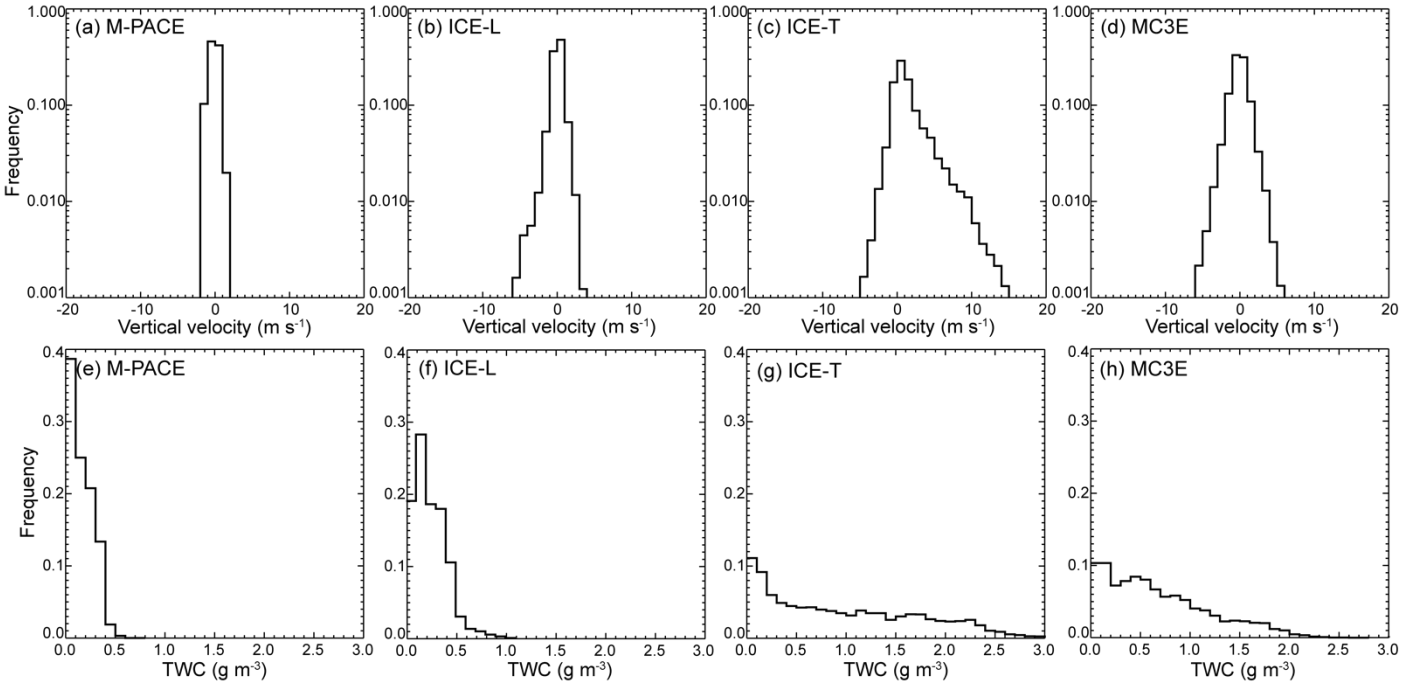


**Figure 3.** Frequency distributions of vertical velocity and TWC sampled in M-PACE, ICE-L, ICE-T, and MC3E, respectively.

An example of ICE-L cloud penetration is shown in Figure 2a–c. It can be seen that the clouds were mostly shallower than 1.5 km. The WCR Ze was typically below 5 dBZ (Figure 2a), indicating a low concentration of large particles. Although the flight-level LWC and the IWC were both low, the LWC was a few times larger than the IWC, resulting in the liquid fraction being mostly higher than 0.6 (Figure 2b). Note that the liquid fraction was low near the lateral edges of the clouds, but these data are not reliable because the LWC was below the lower limit of the King probe, so they were not used in the following statistical analysis. Another property of ICE-L clouds is that wave structures were often seen due to the forcing of the terrain, as indicated by both the WCR Ze and the flight-level vertical velocity (Figure 2c). The frequency distribution of the vertical velocity (Figure 3b) shows that the downdrafts were mostly weaker than $-6$ m s$^{-1}$, and the updrafts were mostly weaker than 4 m s$^{-1}$. Like the Arctic stratiform clouds, the ICE-L clouds had a low TWC (Figure 2f), probably due to the weak updrafts and the shallow cloud depth.

Examples of ICE-T clouds are shown in Figure 2d–f, and the developing, mature, and dissipating stages are marked by the red, orange, and blue boxes. The WCR Ze in the convective cores typically exceeded 15 dBZ, much higher than that in ICE-L clouds. The tops of the ICE-T clouds varied with their life cycle; for mature clouds, the cloud tops could exceed 8 km. According to the sounding measurements, low-level potential instability was observed and the convective available potential energy (CAPE) was higher than 3000 J kg$^{-1}$ during ICE-T. The lifted convection level (LCL) height was approximately 600 m, so the ICE-T clouds were deeper than the Arctic stratiform clouds and the ICE-L clouds. The dynamics were quite different at the three classified stages. The updrafts were strong in convective cores, but weak in dissipating clouds (Figure 2f), thus the frequency distribution of vertical velocity was broad (Figure 3c.) The maximum buoyancy was 0.8 m s$^{-2}$, 0.6 m s$^{-2}$ in developing and mature clouds because of the strong updrafts, while remained lower than 0.4 m s$^{-2}$ in the dissipating clouds. The TWC (Figure 3g) also had a broad frequency distribution in ICE-T clouds, which was high in the convective cores and low in the dissipating clouds. The IWC and the liquid fraction varied with cloud life cycle; in the developing clouds, the observed IWC was low and the liquid fraction was larger

than 0.9, while in the mature and dissipating clouds, the IWC was high and the liquid fraction was lower than 0.5 (Figure 2e).

Figure 2g–i provide an example of an MC3E penetration, including Ze measured using a WSR-88D scanning radar along the flight level. It was observed that the cloud was very deep, with the top of radar echoes higher than 10 km; the true cloud top could be even higher. Strong precipitation was observed, especially between 13:30 UTC and 14:00 UTC, and the IWC was relatively high during this period. The flight-level LWC remained low, thus the liquid fraction was low, especially at about 13:00 when the flight was near the melting layer. The observed vertical velocity varied in the clouds and was mostly weaker than 5 m $s^{-1}$ (Figures 2i and 3d). Because of the presence of a high IWC, the frequency distribution of the TWC was broad compared to the stratiform clouds (Figure 3h) but was narrower than that of ICE-T clouds, due to the lack of strong updrafts.

In short, obvious differences were seen in the characteristics of the clouds sampled during different field campaigns. The Arctic stratiform clouds and the wintertime orographic clouds were mostly shallow, and contained relatively low TWC. In tropical maritime convective clouds, the vertical velocity, and the TWC varied with life cycle, and high TWC was observed in updraft cores. In the stratiform part of MCSs, the TWC and the IWC could be high as well, mainly due to the high cloud tops, but there were no strong updrafts and the LWC was low.

### *3.2. Temperature, Aerosol, Cloud Type, and Life Stage Dependencies of Liquid–Ice Mass Partitions*

Temperature is among the primary factors controlling liquid–ice mass partitioning in mixed-phased clouds, because phase partitioning in mixed-phased clouds is controlled by ice development, which is strongly temperature-related. Many previous studies investigated liquid–ice mass partitioning in mixed-phased clouds as functions of temperature [8,10,13,17,20]. Figure 4 shows the temperature dependency of the mean liquid fractions; the temperatures are the CTT for NSA clouds and the flight-level temperatures for ICE-L, ICE-T, and MC3E clouds. The mean liquid fraction can be calculated in two ways: (1) the mean *LWC* (*LWP*) divided by the mean TWC (TWP) [11]:

$$f_1 = \frac{\overline{LWC}}{\overline{LWC} + \overline{IWC}} \quad or \quad f_1 = \frac{\overline{LWP}}{\overline{LWP} + \overline{IWP}} \tag{2}$$

and (2) the mean of the liquid fractions [9]:

$$f_2 = \overline{\frac{LWC}{LWC + IWC}} \quad or \quad f_2 = \overline{\frac{LWP}{LWP + IWP}} \tag{3}$$

where the bar in the equations indicates averaging. The result derived using the first calculation is helpful when evaluating GCMs with relatively large grid boxes, because GCMs only provide the mean *LWC* (*IWC*) for each big grid, and the result derived in the second calculation can be used to evaluate models with relatively high resolutions that are consistent with the spatial resolution of observations.

The mean liquid fractions calculated in the first way are shown in Figure 4a. For the Arctic stratiform mixed-phase clouds sampled at NSA, the annual mean liquid fractions decreased from approximately 1 to 0.6 as the CTT decreased from 0 °C to −30 °C, consistent with a previous study of Arctic mixed-phase clouds based on ground-based remote sensing measurements [13]. The relatively high fractions are due to the low ice concentrations at temperatures warmer than −15 °C in non-spring seasons [28,40] and the short residence time of ice particles in the mixed-phase layers. If the precipitating layers are included, the liquid fractions are lower than those shown in Figure 4a. In spring, the liquid fractions in NSA clouds decreased from approximately 0.9 to 0.2, while the CTT decreased from −12 °C to −30 °C, whereas in other seasons, the liquid fraction varied between 0.6 and 1. This is probably because there is more dust in spring than in the other seasons in Barrow, Alaska, which serve as efficient ice-nucleating particles (INP) at temperatures below −15 °C [5,41].

Using MPL measurements at the NSA site, Zhao [42] showed that the occurrence of dust had a maximum value in spring (~12%) and a minimum value in autumn (less than 2%). Satellite measurements have also shown a higher occurrence of dust in spring than in other seasons in the Arctic [43].

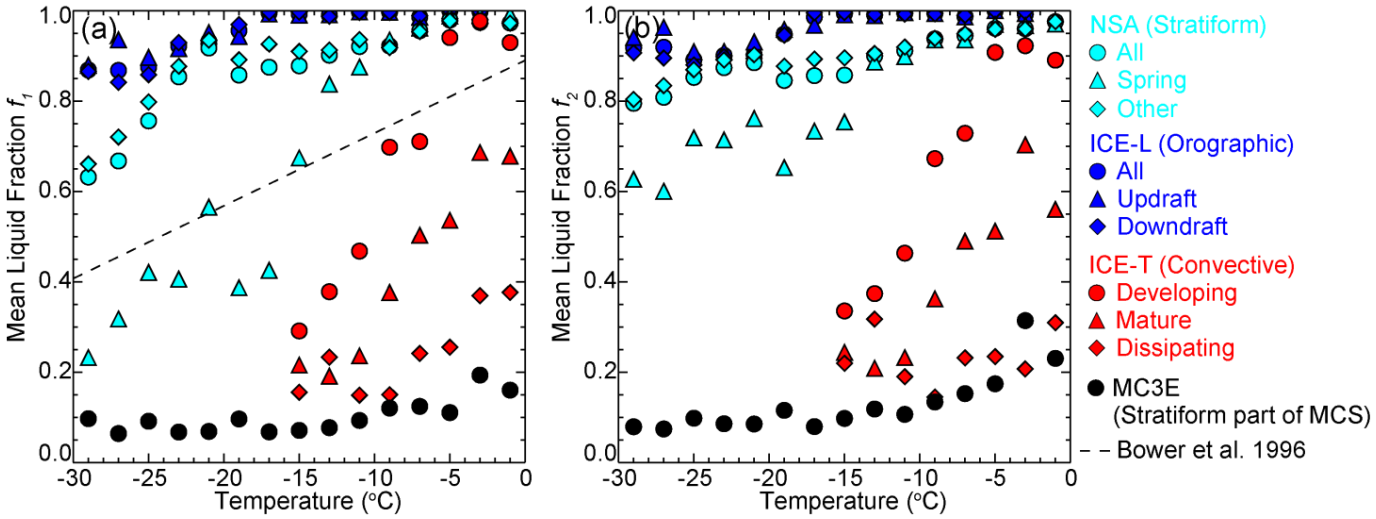


**Figure 4.** (**a**) Mean liquid fractions as a function of temperature for stratiform clouds sampled at the NSA site, orographic clouds sampled in ICE-L, tropical maritime convective clouds sampled in ICE-T, and stratiform parts of MCSs sampled in MC3E, as well as a parameterization from a previous study. The mean liquid fractions were calculated using Equation (1) for every 2 °C. (**b**) Similar to (**a**), but the mean liquid fractions were calculated using Equation (2).

The mean liquid fraction in wintertime orographic clouds sampled during ICE-L was slightly higher than that of NSA clouds during non-spring seasons. The high liquid fraction is probably a result of low ice concentration and the relatively low residence time of air parcels moving through the orographic (mostly wave) clouds. The concentration of ice larger than 100 μm in ICE-L clouds is low (0.1–10 $L^{-1}$, not shown), consistent with the ice concentration in Arctic stratiform clouds during non-spring seasons [28]. If the temperatures inside clouds are used for the NSA clouds, the liquid fraction for the NSA clouds would be even lower (i.e., a larger difference in liquid fraction between the NSA and ICE-L clouds). The mean liquid fractions in updrafts slightly exceeded that in downdrafts in ICE-L clouds between −30 °C and −20 °C, but the differences were small. Here, we simply defined an updraft as an ascending cloud parcel with a flight-level vertical velocity greater than 0.2 m $s^{-1}$ and a downdraft as a descending parcel with a flight-level vertical velocity less than −0.2 m $s^{-1}$. In wave clouds (e.g., lenticular clouds), ice grows along the stream flow, and larger ice mass fractions and pure ice regions may be observed in downdrafts [29,44]. In this study, a threshold of LWC > 0.05 g $m^{-3}$ was applied, so ice clouds (regions) were not included.

Liquid–ice mass partitioning in convective clouds is very different than that in stratiform clouds. As shown in Figure 4a, the liquid fraction in the developing convective clouds sampled during ICE-T decreased from approximately 1 to 0.3 as the temperature decreased from 0 °C to −15 °C. Updraft cores in ICE-T clouds typically have a mean vertical velocity greater than 2 m $s^{-1}$, so assuming the updraft core increases adiabatically with a moist lapse rate of 6 K $km^{-1}$, as estimated from sounding measurement, it takes less than 1250 s for the liquid fraction to decrease from about 1 to 0.3, suggesting the liquid–ice mass partitioning in the developing convective clouds was controlled by fast ice generation, and the liquid fraction decreases much faster than that in Arctic stratiform clouds. If the temperature inside clouds is used for NSA clouds, the liquid fraction for the NSA clouds would be lower, but this impact is not significant given the relatively shallow cloud depth of Arctic stratiform clouds, which is typically less than 800 m. In addition, in developing convective

clouds, the flight-level temperatures are close to the CTTs. Therefore, the different temperature definitions do not change this conclusion. In convective clouds, the presence of drizzle-size and millimeter drops are an important source of rapid ice generation [17,45–48], and secondary ice production enhances ice generation in convective clouds [15,46]. Phase partitioning in convective clouds also varies significantly as the clouds evolve. At mature stage, the liquid fractions were lower than in developing clouds, due to the strong liquid–ice interaction and the secondary ice production, especially at warmer temperatures (>−10 °C). In the dissipating stage, the clouds were dominated by ice, and the liquid fractions decreased from 0.4 to 0.15 as the temperature decreased from 0 °C to −15 °C (Figure 4a); the low liquid fraction was due to the strong liquid–ice interaction and the lack of updrafts and water vapor. Considering the uncertainty associated with the drop-identification algorithm, the liquid fractions in dissipating clouds may be even lower [17].

The clouds sampled in ICE-T were mostly isolated convective clouds, whereas the liquid–ice mass partitioning in MCSs may be different than for isolated convection. Figure 4a suggests that the mean liquid fractions in the clouds sampled during MC3E were generally lower than 0.2 between 0 °C and −30 °C. As mentioned earlier, the penetrations made in MC3E were mostly in stratiform parts of the MCSs, in which the dynamics were more similar to those of the dissipating clouds in ICE-T than to those of the developing and mature clouds, and the flight levels were typically far below the cloud tops.

A temperature-dependent liquid fraction parameterization from a previous study [20] is shown in Figure 4a. This parameterization was developed largely based on measurements in mid-latitude continental cumulus clouds. The obvious differences in the liquid fractions between ICE-T clouds and Bower's parameterization reveal the potential systematic differences in phase partitioning between maritime and continental convective clouds.

The temperature-dependent mean liquid fractions calculated using Equation (2) are shown in Figure 4b. The results are similar to those shown in Figure 4a, except for NSA clouds between −20 °C and −30 °C in spring. This is because the liquid fraction is bimodally distributed (Figure 5). High liquid fractions (>0.8) were more frequently observed in NSA clouds between −20 °C and −30 °C, but clouds with low liquid fractions (< 0.2) often had a relatively large TWP, as shown in Figure 5. In the first averaging method, the larger TWP had a higher weighting than the smaller TWP, while in the second method, different TWPs had the same weighting, so the liquid fraction averaged using the first method was lower than that using the second method. The frequency of liquid fractions in NSA clouds during spring better showed the high occurrence of liquid-dominated clouds (regions) between −30 °C and 0 °C, and the occurrence of ice-dominated clouds (regions) increased as the CTT decreased from −15 °C to −30 °C. This will be discussed in more detail in Section 3.2.

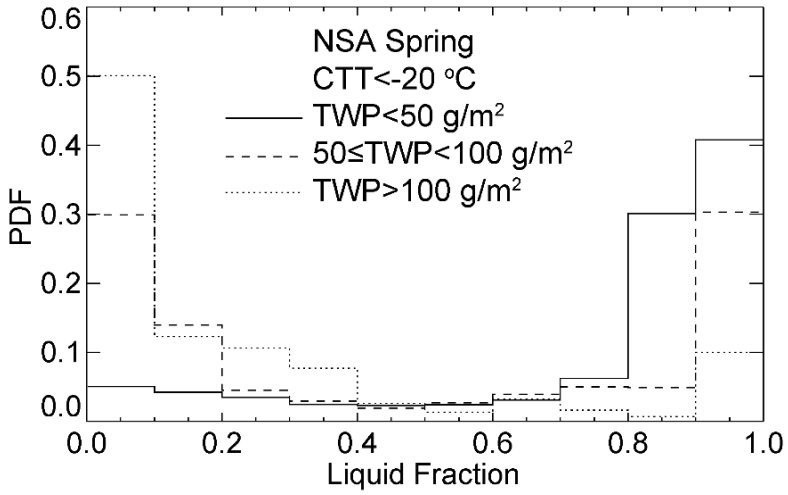


**Figure 5.** PDF of the liquid fractions for NSA clouds with CTTs below −20 °C during spring.

Although the liquid fractions in the Arctic stratiform clouds in Figures 4 and 5 were derived based on remote sensing techniques, their magnitude was consistent with the airborne measurement in a stratiform cloud sampled in the same area. Figure 6 shows the liquid fractions from in situ airborne measurements through spiral penetrations in a single-layer mixed-phase stratiform cloud in the Arctic on 9, 10, and 12 October 2004. As seen in the figure, the mean liquid fraction decreased from 1 to 0.6 from cloud top to cloud base; this was because the ice initiated near the cloud top and diminished as the ice grew [28]. The temperature dependencies of the liquid fractions were different from those shown in Figure 4 and in this Arctic case (Figure 6) because of the different sampling methods, i.e., random sampling of multiple clouds in Figure 4 compared with the spiral penetrations at multiple layers in a single cloud in Figure 6. Unlike ground-based remote sensing measurements (Figure 4), the mean liquid fractions calculated using the two different methods had no significant difference, because in situ measurements cannot reveal the cloud thickness and TWP. Taking into account the sampling differences at different levels, the overall average liquid fraction was about 0.86, consistent with the magnitude of the liquid fraction from ground-based remote sensing measurements during non-spring seasons, and with the magnitude measured during ICE-L. The fact that the liquid fractions in the Arctic stratiform clouds, measured by different techniques, had similar magnitudes provided us with confidence that the phase partitioning were very different in stratiform clouds and convective clouds at different stages, indicating that phase partitioning is strongly dependent on cloud type and life stage.

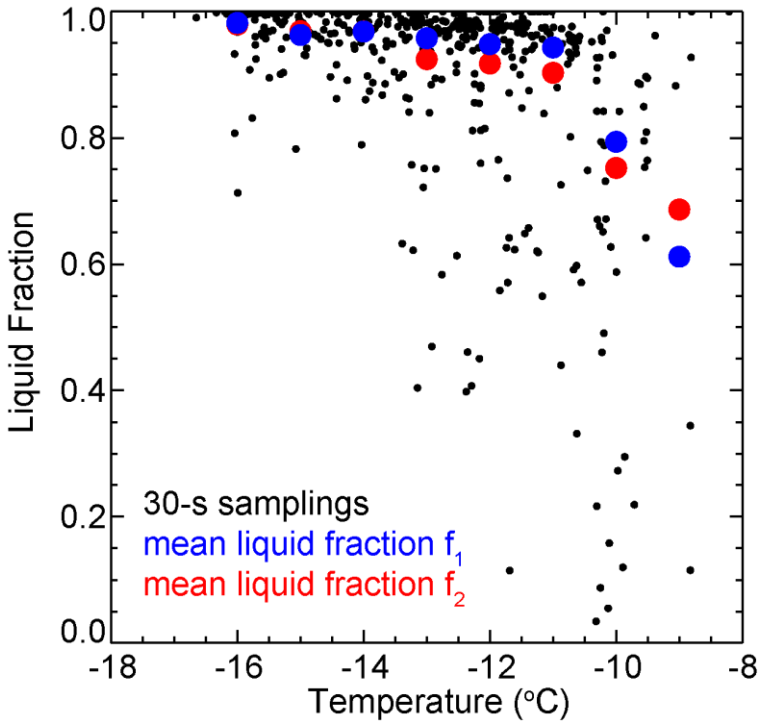


**Figure 6.** Liquid fraction in the mixed-phase stratiform cloud sampled at NSA site by UND Citation aircraft on 9, 10, and 12 October 2010. The black dots indicate the 30-s samplings, and the big blue and red dots indicate the mean liquid fractions calculated using Equations (1) and (2), respectively.

### *3.3. Variability of the Liquid Fractions*

In addition to the mean of the temperature-dependent liquid fractions, it is also important to understand their variability [6]. Figure 7 shows the standard deviations of the liquid fraction for every 2 °C temperature interval. For NSA and ICE-L clouds, the standard deviations generally increased with decreasing temperature, and the larger standard deviations were associated with lower mean liquid fractions, suggesting that the glaciation process resulted in larger variability of phase partitioning in stratiform clouds.

For ICE-T developing convective clouds, the standard deviations of the liquid fractions increased and then decreased with decreasing temperature; the maximum value was found at approximately −7 °C. For mature and dissipating ICE-T clouds as well as MC3E clouds, the standard deviations of the liquid fractions decreased with decreasing temperature. Similar trends and magnitudes of the standard deviations of the liquid fractions were also found in a similar plot for a temperature interval of 1 °C (not shown). The different temperature dependencies of the variability of phase partitioning, as shown in Figure 7, indicated different glaciation processes in stratiform and convective clouds.

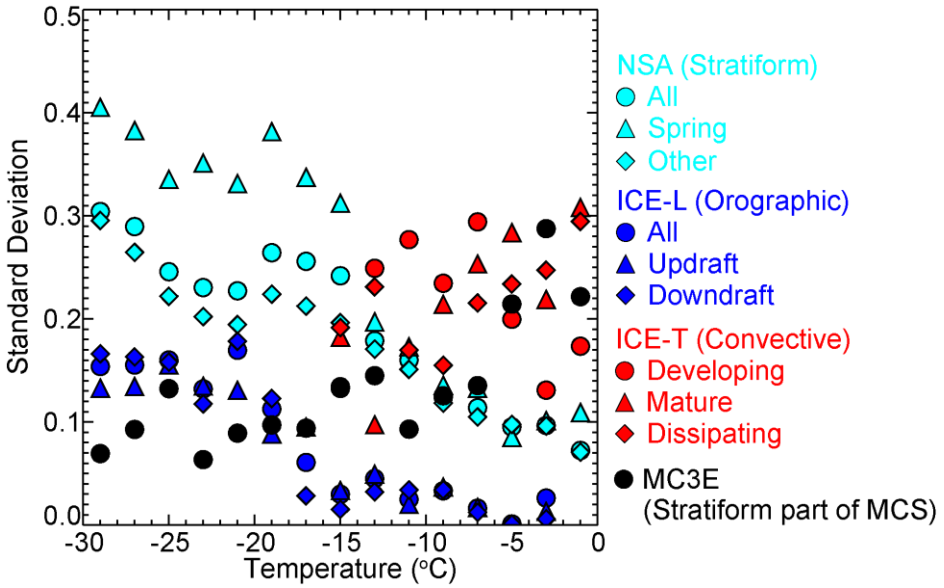


**Figure 7.** Standard deviations of the liquid fractions for stratiform mixed-phase clouds sampled at the NSA site, orographic mixed-phase clouds sampled in ICE-L, tropical maritime convective clouds sampled in ICE-T, and stratiform parts of MCSs sampled in MC3E.

To better understand the variability of liquid–ice mass partitioning in mixed-phase clouds, we plotted the frequencies of the liquid fractions, as shown in Figure 8. For Arctic stratiform clouds (Figure 8a–c), the liquid fractions were mostly higher than 0.8 at warm temperatures (>10 °C). As the temperature decreased, the occurrence frequency of the mixed-phase regions and the ice-dominated regions both increased. However, the frequency of the mixed-phase region obtained less increase compared to that of ice-dominated region, results in a bimodal distribution of liquid fraction at temperature colder than −15 °C. That pattern was clearer during spring (Figure 8a), which explains the increasing standard deviation of the liquid fractions with decreasing temperature (Figure 7). The frequency distribution of the liquid fractions in Arctic stratiform clouds shown in this study is consistent with that reported in [8], which also showed relatively high frequencies of high (>0.9) or (and) low (<0.1) liquid fractions in mixed-phase stratiform clouds using in situ measurements. This indicates that the glaciation time of any cloud region with abundant ice is usually less than the characteristic residence time of liquid water in stratiform clouds.

The variability of liquid fractions in convective clouds sampled in ICE-T had a different temperature dependency compared to that of the Arctic stratiform clouds. As seen in Figure 8e, the frequency distribution of liquid fractions continuously shifted from the liquid-dominated pattern to the ice-dominated pattern as the temperature decreased. No bimodal distribution was seen in any temperature range, suggesting a continuous glaciation process in the vertical development of convective clouds. Between −12 °C and −5 °C, the frequency distributions of the liquid fractions were broad, whereas at warmer or colder temperatures the frequency distributions were relatively narrow; this explains why the standard deviation of the liquid fractions in developing convective clouds (Figure 7)

increased and then decreased with decreasing temperature, and indicates a highly variable phase partitioning in the mixed-phase regions, probably due to a combination of multiple causes such as strong turbulence and complicated liquid–ice interactions. The frequency distribution of the liquid fractions in the mature convective clouds sampled in ICE-T (Figure 8f) was broader at warm temperatures than for developing convective clouds and narrowed towards the low-liquid fraction side, indicating a higher occurrence of mixed-phase regions at warm temperatures due to the fall of ice. The dissipating clouds sampled in ICE-T (Figure 8g) were dominated by ice, and the liquid fractions were mostly low.

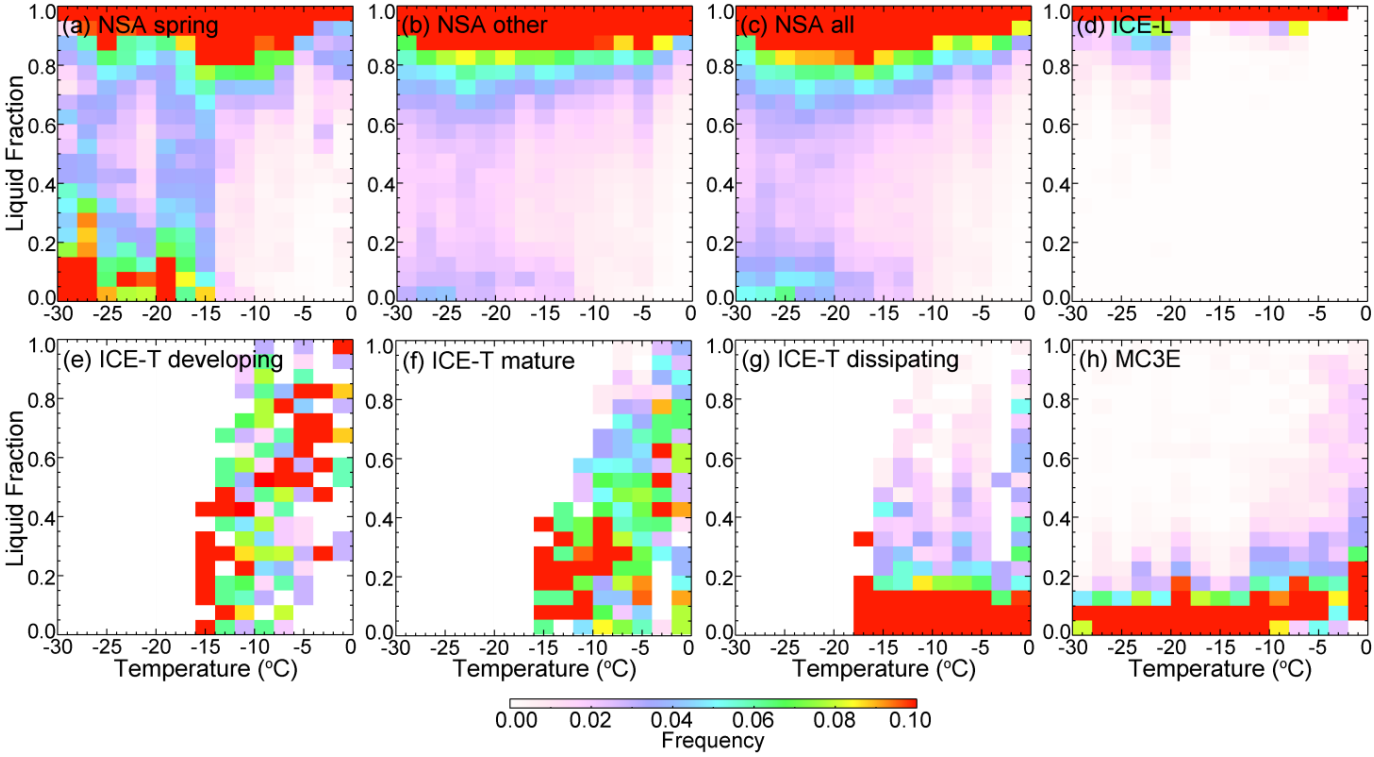


**Figure 8.** Frequencies of the liquid fractions in mixed-phase clouds sampled over NSA using ground-based remote sensors, and the frequencies during ICE-L, ICE-L and MC3E using aircraft in situ measurements.

The different temperature-dependent distributions of liquid fractions in stratiform and convective clouds revealed their different glaciation processes. In the Arctic stratiform clouds, the ice grew mainly through the Wegener-Bergeron-Findeisen (WBF) process. If there was sufficient ice, the liquid water was rapidly consumed, as indicated by the bimodal distribution in Figure 8e, while in developing convective clouds, although the phase partitioning was controlled by fast ice generation, the strong updrafts continuously provided water vapor for drop growth, resulting in a higher occurrence of mixed-phase regions. Thus, the phase partitioning in convective clouds not only depends on the ice generation, but also on the growth rates of drops and ice, as well as the liquid–ice interactions. If no strong updraft was present, the liquid water could be rapidly consumed.

The wintertime orographic clouds sampled in ICE-L (Figure 8d) were dominated by liquid water, and the frequency distribution of the liquid fractions slightly broadened with decreasing temperature. It is not clear why there was no bimodal distribution of liquid fraction observed in ICE-L clouds; a possible reason is that the ice concentration was low and there was not enough time for the liquid water to be consumed as the wave clouds evolved from the upwind side to the lee side. The glaciation time of wave clouds may be controlled by both the microphysics and the gravity of waves induced by the terrain. The MC3E clouds (Figure 8h) were dominated by ice in all temperature ranges because of the high cloud top and the fall of ice, so the liquid fraction was low and its frequency distribution was mostly narrow.

## 4. Discussion

The cloud type and life cycle dependencies of liquid–ice mass partitioning in mixed-phase clouds were analyzed in this study using ground-based remote sensing measurements and aircraft in situ measurements. The results are useful in evaluating and improving model simulations, especially GCMs [6]. Tan et al. [6] showed that the cloud-phase feedback on climate is highly sensitive to the liquid fraction in mixed-phase clouds. However, the liquid fraction is significantly biased in GCM, due to the coarse resolution and the poorly represented microphysics [6,49]. Typically, it is assumed that the liquid and ice are homogeneously mixed in a grid box in GCM [50], but based on the results shown in this paper, the liquid fraction is highly variable in the clouds. The modelled life cycle of mixed-phase clouds also has large uncertainties in GCM [50], resulting in a poor performance in simulating the phase transition of mixed-phase clouds. This is mainly because the ice microphysics is not well parameterized, as indicated by the overestimated ice growth rate through the WBF process [6] and the underestimated ice multiplication in convective clouds [45,47,48]. Therefore, it is important to use observations to constrain model simulations and to improve parameterizations.

There are still remaining questions. First, clouds that are not analyzed in this paper may have different characteristics of phase partitioning. Deep stratiform clouds formed due to a front system may have higher ice concentration due to the higher cloud tops, leading to a lower liquid fraction compared to that shown in this paper [18]. Convective clouds over land and ocean have different dynamics and aerosol loading; thus, they may experience different life cycles and glaciation processes [16,26,48]. Liquid fractions in the updraft cores of deep moist convection are still not well known; this requires measurements using storm-penetrating aircrafts, which are still limited. Phase partitioning in mixed-phase clouds also vary at different geolocations around the world, depending on water vapor condition, aerosols' properties, and the source of INPs [51]. A more comprehensive analysis using data sampled in different areas and under different weather conditions would be helpful in improving our understanding of the cloud-type dependencies of phase partitioning in mixed-phase clouds.

In addition, the broad frequency distributions of the liquid fractions indicated that the liquid–ice mass partitioning was highly variable, and the variability had different temperature dependencies for different cloud types. The main factors controlling the variability are not known, and could be a result of multiple causes. For example, aerosols are an important factor that control ice initiation [36] in mixed-phase clouds, but aerosol concentrations and chemical properties are highly variable [5,36]. Secondary ice generation is more important in convective clouds [17], and there may be several different secondary ice-generation mechanisms, with efficiencies that vary with ambient conditions. For example, the drop freezing-splinter mechanism is more efficient between −8 °C and −25 °C [45,47,48], whereas the riming-splinter process is more efficient between −3 °C and −8 °C [46]. Secondary ice production is also related to other ambient conditions, including vertical velocity [15]. Dynamics also impact the phase partitioning in mixed-phase stratiform and convective clouds [52]. Shupe et al. [10] suggested that the LWP and the IWP in Arctic stratiform mixed-phase clouds increase with increasing vertical velocity, whereas liquid fractions decrease as vertical velocity increases. Yang et al. [17] suggested that in developing convective clouds, the LWC, the IWC, and the liquid fractions are higher in stronger updrafts, but the vertical velocity dependence on the liquid fraction in convective clouds is minor compared to the temperature and life stage dependencies. Turbulence also enhances ice generation and the variability of phase partitioning in mixed-phase clouds [53], especially in convective clouds, in which strong turbulence is often observed [16].

The quantitative results shown in this study could be improved in the future with more advanced instruments and more measurements. For aircraft in situ measurements, the LWC measured by a King probe has a lower limit of 0.05 g $m^{-3}$; this excludes the cloud regions with extremely low water content, such as the cloud edges. The IWC in ICE-L, M-PACE, and MC3E was derived using the mass-size relationship of ice, and did not

include the mass carried by small ice (<100 μm), both of which may induce uncertainties in the derived IWC, but this cannot be verified since there is no ground truth measurement. A TWC probe such as the CVI could be more reliable in estimating the IWC if the LWC is accurate and the TWC is within the detection range of the probe. For ground-based remote sensing, the uncertainty mainly came from the assumptions made in the retrieval method, such as the PSD of the ice and the shape of the ice particles. These assumptions may be improved by using more recent aircraft measurements and taking into account the differences in the ice properties among different types of clouds. Another limitation of ground-based remote sensing is its limited horizontal detection range, although it is powerful in investigating the vertical structure of clouds. Therefore, it is necessary to apply the retrieval method to satellites to improve the sample size.

## 5. Conclusions

The phase partitioning in mixed-phase clouds spanning tropics, midlatitudes, and the Arctic was investigated in this study, using data collected from six years of ground-based remote sensing measurements at the NSA site and aircraft in situ measurements in three field campaigns. The temperature, cloud type, and life cycle dependencies of phase partitioning were qualitatively analyzed, and the variability of liquid–ice mass partitioning in different cloud types and life stages were discussed. The main findings are listed as follows.

(1) Ground-based remote sensing measurements show the liquid fraction in Arctic stratiform clouds decreased from 1 to 0.6 (or 0.8, depending on the definition of liquid fraction) between 0 °C and −30 °C, and was lower in spring between −15 °C and −30 °C because of the higher dust occurrence in Barrow, Alaska. Aircraft measurements in the Arctic stratiform clouds indicated a similar magnitude of liquid fraction when compared to the remote sensing measurements, suggesting that the liquid fraction decreased from cloud top to base due to the fall of ice particles.

(2) In wintertime orographic clouds sampled over the Rocky Mountains, the mean liquid fraction decreased with decreasing temperature, but remained greater than 0.8 between 0 °C and −30 °C; this was observed in both the upwind side and the lee side.

(3) Phase partitioning in tropical maritime convective clouds strongly depends on life stages. In the developing stage, it decreased from 1 to 0.3 between −5 °C and −15 °C, indicating rapid ice generation, while at the mature stage, the liquid fractions were lower due to falling ice and liquid–ice interactions. At the dissipating stage, the clouds were mostly dominated by ice, so the liquid fraction was lower than 0.4.

(4) In the stratiform regions of midlatitude MCSs, the liquid fraction was lower than 0.3 between 0 °C and −30 °C, indicating that ice dominated in all temperature ranges above the melting level.

(5) The phase partitioning in mixed-phase clouds was highly variable, and the frequency distributions of the liquid fractions differed for different types of clouds, suggesting different glaciation processes in stratiform and convective clouds. In stratiform clouds, liquid dominated at warm temperatures. As the temperature decreased, an ice-dominated region was more frequently observed, while the occurrence of the mixed-phase region remained low. For convective clouds, the variability of phase partitioning was controlled by continuous glaciation with decreasing temperature and life cycle.

The results highlight that temperature-dependent phase partitioning varies significantly among different cloud types and needs to be better parameterized in models. Future works include investigation of phase partitioning in cloud types that are not presented in this paper, such as deep convective clouds and frontal systems; a better understanding of the factors controlling the variability of liquid fraction in different cloud types; and evaluation of model simulations as well as improvement of the parameterizations using observations.

**Author Contributions:** Conceptualization, J.Y. and Z.W.; methodology, J.Y.; software, J.Y., Y.Z. and Z.W.; validation, J.Y., Y.Z., Z.W. and D.Z.; formal analysis, J.Y.; investigation, J.Y., Z.W. and D.Z.; resources, J.Y. and Z.W.; data curation, J.Y. and Z.W.; writing—original draft preparation, J.Y.; writing—

review and editing, J.Y., Y.Z., Z.W. and D.Z.; visualization, J.Y.; supervision, Z.W.; project administration, J.Y. and Z.W.; funding acquisition, J.Y. and Z.W. All authors have read and agreed to the published version of the manuscript.

**Funding:** This work was funded by the National Key Research and Development Program of China, Grant No. 2019YFC0214604, the National Natural Science Foundation of China, Grant No. 41905124, 42005064, the Natural Science Foundation of Jiangsu Province, China, Grant No. BK20190778 and BK20190777, Shanghai Typhoon Research Foundation TFJJ202001, NSF awards ATM-0612605 and AGS-1034858, and DOE Grant DE-SC0006974 as part of the ASR program.

**Data Availability Statement:** The NSA datasets were obtained from the Atmospheric Radiation Measurement data archive (http://www.archive.arm.gov/) (accessed on 25 January 2022). The ICE-L dataset was obtained from the NCAR ICE-L data archive (www.eol.ucar.edu/field_projects/ice-l) (30 January 2022). The ICE-T dataset was obtained from the NCAR ICE-T data archive (www.eol.ucar.edu/field_projects/ice-t) (accessed on 15 January 2022). The UND Citation data for MC3E can be obtained from the NASA data archive (https://data.nasa.gov) (accessed on 15 January 2022).

**Acknowledgments:** The authors wish to thank the NSF/NCAR C-130 and UND Citation II crews for collecting and processing the aircraft data. We appreciate the insightful comments and suggestions of Andrew Heymsfield of NCAR and four anonymous reviewers, which greatly improved the manuscript.

**Conflicts of Interest:** The authors declare no conflict of interest.

## References

1. Stocker, T.F.; Qin, D.; Plattner, G.K.; Tignor, M.M.; Allen, S.K.; Boschung, J.; Nauels, A.; Xia, Y.; Bex, V.; Midgley, P.M. *Climate Change 2013: The Physical Science Basis. Contribution of Working Group I to the Fifth Assessment Report of the Intergovernmental Panel on Climate Change*; Cambridge University Press: Cambridge, UK.; New York, NY, USA, 2013; p. 1535. [CrossRef]
2. de Boer, G.; Chapman, W.; Kay, J.E.; Medeiros, B.; Shupe, M.D.; Vavrus, S.; Walsh, J. A characterization of the present-day Arctic atmosphere in CCSM4. *J. Clim.* **2012**, *25*, 2676–2695. [CrossRef]
3. Khain, A.P.; Beheng, K.D.; Heymsfield, A.; Korolev, A.; Krichak, S.O.; Levin, Z.; Pinsky, M.; Phillips, V.; Prabhakaran, T.; Teller, A.; et al. Representation of microphysical processes in cloud-resolving models: Spectral (bin) microphysics versus bulk parameterization. *Rev. Geophys.* **2015**, *53*, 247–322. [CrossRef]
4. Zhao, M.; Wang, Z. Comparison of Arctic clouds between European Center for Medium-Range Weather Forecasts simulations and Atmospheric Radiation Measurement Climate Research Facility long-term observations at the North Slope of Alaska Barrow site. *J. Geophys. Res.* **2010**, *115*, D23202. [CrossRef]
5. DeMott, P.J.; Prenni, A.J.; Liu, X.; Kreidenweis, S.M.; Petters, M.D.; Twohy, C.H.; Richardson, M.S.; Eidhammer, T.; Rogers, D. Predicting global atmospheric ice nuclei distributions and their impacts on climate. *Proc. Natl. Acad. Sci. USA* **2010**, *107*, 11217–11222. [CrossRef]
6. Tan, I.; Storelvmo, T.; Zelinka, M. Observational constraints on mixed-phase clouds imply higher climate sensitivity. *Science* **2016**, *352*, 224–227. [CrossRef]
7. Tan, I.; Storelvmo, T. Sensitivity study on the influence of cloud microphysical parameters on mixed-phase cloud thermodynamic phase partitioning in CAM5. *J. Atmos. Sci.* **2016**, *73*, 709–728. [CrossRef]
8. Korolev, A.; Isaac, G.; Cober, S.G.; Strapp, J.W.; Hallett, J. Microphysical characterization of mixed-phase clouds. *Qt. J. R. Meteorol. Soc.* **2003**, *129*, 39–65. [CrossRef]
9. Wang, Z.; Sassen, K. Cirrus cloud microphysical property retrieval using lidar and radar measurements. Part I: Algorithm description and comparison with in situ data. *J. Appl. Meteorol.* **2002**, *41*, 218–229. [CrossRef]
10. Shupe, M.D.; Matrosov, S.Y.; Uttal, T. Arctic mixed-phase cloud properties derived from surface-based sensors at SHEBA. *J. Atmos. Sci.* **2006**, *63*, 697–711. [CrossRef]
11. Jing, X.; Geerts, B.; Wang, Y.; Liu, C. Evaluating seasonal orographic precipitation in the Interior Western United States using gauge data, gridded precipitation estimates, and a regional climate simulation. *J. Hydrometeorol.* **2017**, *18*, 2541–2558. [CrossRef]
12. Shupe, M.D.; Kollias, P.; Persson, P.O.G.; McFarquhar, G.M. Vertical motions in Arctic mixed-phase stratiform clouds. *J. Atmos. Sci.* **2008**, *65*, 1304–1322. [CrossRef]
13. de Boer, G.; Eloranta, E.W.; Shupe, M.D. Arctic mixed-phase stratiform cloud properties from multiple years of surfacebased measurements at two high-latitude locations. *J. Atmos. Sci.* **2009**, *66*, 2874–2887. [CrossRef]
14. Zhang, D.; Wang, Z.; Liu, D. A global view of midlevel liquid-layer topped stratiform cloud distribution and phase partition from CALIPSO and CloudSat measurements. *J. Geophys. Res.* **2010**, *115*, D00H13. [CrossRef]
15. Heymsfield, A.; Willis, P. Cloud conditions favoring secondary ice particle production in tropical maritime convection. *J. Atmos. Sci.* **2014**, *71*, 4500–4526. [CrossRef]
16. Yang, J.; Wang, Z.; Heymsfield, A.; French, J. Characteristics of Vertical Air Motion in Isolated Convective Clouds. *Atmos. Chem. Phys.* **2016**, *16*, 10159–10173. [CrossRef]

17. Yang, J.; Wang, Z.; Heymsfield, A.; Luo, T. Liquid–Ice Mass Partition in Tropical Maritime Convective Clouds. *J. Atmos. Sci.* **2016**, *73*, 4959–4978. [CrossRef]
18. Roeckner, E.; Brokopf, R.; Esch, M.; Giorgetta, M.A.; Hagemann, S.; Kornblueh, L.; Manzini, E.; Schlese, U.; Schulzweida, U. Sensitivity of Simulated Climate to Horizontal and Vertical Resolution in the ECHAM5 Atmosphere Model. *J. Clim.* **2006**, *19*, 3771–3791. [CrossRef]
19. Cantrell, W.; Heymsfield, A. Production of ice in tropospheric clouds: A review. *Bull. Am. Meteorol. Soc.* **2005**, *86*, 795–807. [CrossRef]
20. Bower, K.; Moss, S.J.; Johnson, D.W.; Choularton, T.W.; Latham, J.; Brown, P.R.A.; Blyth, A.M.; Cardwell, J. A parametrization of ice water content observed in frontal and convective clouds. *Q. J. R. Meteorol. Soc.* **1996**, *122*, 1815–1844. [CrossRef]
21. Yang, J.; Wang, Z.; Heymsfield, A.J. On the Freezing Time of Supercooled Drops in Developing Convective Clouds over Tropical Ocean. *Atmos. Res.* **2018**, *211*, 30–37. [CrossRef]
22. Yang, J.; Wang, Z.; Heymsfield, A.J.; DeMott, P.J.; Twohy, C.H.; Suski, K.J.; Toohey, D.W. High ice concentration observed in tropical maritime stratiform mixed-phase clouds with top temperatures warmer than −8 °C. *Atmos. Res.* **2020**, *233*, 104719. [CrossRef]
23. Wang, J.; Dong, X.; Xi, B. Investigation of ice cloud microphysical properties of DCSs using aircraft in situ measurements during MC3E over the ARM SGP site. *J. Geophys. Res. Atmos.* **2015**, *120*, 3533–3552. [CrossRef]
24. Morrison, H.; de Boer, G.; Feingold, G.; Harrington, J.; Shupe, M.D.; Sulia, K. Resilience of persistent Arctic mixed-phase clouds. *Nat. Geosci.* **2012**, *5*, 11–17. [CrossRef]
25. Boudala, F.S.; Isaac, G.A.; Cober, S.G.; Fu, Q. Liquid fraction in stratiform mixed-phase clouds from in situ observations. *Q. J. R. Meteorol. Soc.* **2004**, *130*, 2919–2931. [CrossRef]
26. Heymsfield, G.M.; Tian, L.; Heymsfield, A.J.; Li, L.; Guimond, S. Characteristics of Deep Tropical and Subtropical Convection from Nadir-Viewing High-Altitude Airborne Doppler Radar. *J. Atmos. Sci.* **2010**, *67*, 285–308. [CrossRef]
27. Wang, Z.; Sassen, K. Cirrus cloud microphysical property retrieval using lidar and radar measurements. Part II: Midlatitude cirrus microphysical and radiative properties. *J. Atmos. Sci.* **2002**, *59*, 2291–2302. [CrossRef]
28. McFarquhar, G.M.; Zhang, G.; Poellot, M.R.; Kok, G.L.; McCoy, R.; Tooman, T.; Fridlind, A.; Heymsfield, A.J. Ice properties of single-layer stratocumulus during the Mixed-Phase Arctic Cloud Experiment: 1. *Obs. J. Geophys. Res.* **2007**, *112*, D24201. [CrossRef]
29. Heymsfield, A.J.; Field, P.R.; Bailey, M.; Rogers, D.; Stith, J.; Twohy, C.; Wang, Z.; Haimov, S. Ice in clouds experiment—Layer clouds. Part I: Ice growth rates derived from lenticular wave cloud penetrations. *J. Atmos. Sci.* **2011**, *68*, 2628–2654. [CrossRef]
30. Khanal, S.; Wang, Z. Evaluation of the Lidar–Radar Cloud Ice Water Content Retrievals Using Collocated in Situ Measurements. *J. Appl. Meterol. Climatol.* **2015**, *54*, 2087–2097. [CrossRef]
31. Wang, Z. A refined two-channel microwave radiometer liquid water path retrieval for cold regions by using multiple-sensor measurements. *IEEE Geosci. Remote Sens. Lett.* **2007**, *4*, 591–595. [CrossRef]
32. Troyan, D. *Merged Sounding Value-Added Product. Technical Report*; DOE ARM Office of Science: Washington, DC, USA, 2012.
33. Protat, A.; Bouniol, D.; O'Connor, E.J.; Klein Baltink, H.; Verlinde, J.; Widener, K. CloudSat as a global radar calibrator. *J. Atmos. Ocean. Technol.* **2011**, *28*, 445–452. [CrossRef]
34. King, W.D.; Parkin, D.A.; Handsworth, R.J. A hot-wire liquid water device having fully calculable response characteristics. *J. Appl. Meteorol.* **1978**, *17*, 1809–1813. [CrossRef]
35. Locatelli, J.D.; Hobbs, P.V. Fall speeds and masses of solid precipitation particles. *J. Geophys. Res.* **1974**, *79*, 2185–2197. [CrossRef]
36. Hogan, R.J.; Tian, L.; Brown, P.R.; Westbrook, C.D.; Heymsfield, A.J.; Eastment, J.D. Radar Scattering from Ice Aggregates Using the Horizontally Aligned Oblate Spheroid Approximation. *J. Appl. Meteorol. Climatol.* **2022**, *51*, 655–671. [CrossRef]
37. Brown, P.R.A.; Francis, P.N. Improved Measurements of the Ice Water Content in Cirrus Using a Total-Water Probe. *J. Atmos. Ocean. Technol.* **1995**, *12*, 410–414. [CrossRef]
38. Twohy, C.H.; Schanot, A.J.; Cooper, W.A. Measurement of condensed water content in liquid and ice clouds using an airborne counterflow virtual impactor. *J. Atmos. Ocean. Technol.* **1997**, *14*, 197–202. [CrossRef]
39. LeMone, M.A.; Zipser, E.J. Cumulonimbus vertical velocity events in GATE. Part I: Diameter, intensity and mass flux. *J. Atmos. Sci.* **1980**, *37*, 2444–2457. [CrossRef]
40. Jackson, R.C.; McFarquhar, G.M.; Korolev, A.V.; Earle, M.E.; Liu, P.S.; Lawson, R.P.; Brooks, S.; Wolde, M.; Laskin, A.; Freer, M. The dependence of ice microphysics on aerosol concentration in arctic mixed-phase stratus clouds during ISDAC and M-PACE. *J. Geophys. Res. Atmos.* **2012**, *117*, D15. [CrossRef]
41. Murray, B.J.; O'Sullivan, D.; Atkinson, J.D.; Webb, M.E. Ice nucleation by particles immersed in supercooled cloud droplets. *Chem. Soc. Rev.* **2012**, *41*, 6519–6554. [CrossRef]
42. Zhao, M. *The Arctic Clouds from Model Simulations and Long-Term Observations at Barrow, Alaska*; Doctoral Dissertation, University of Wyoming: Laramie, WY, USA, 2011; p. 178.
43. Luo, T.; Wang, Z.; Zhang, D.; Liu, X.; Wang, Y.; Yuan, R. Global dust distribution from improved thin dust layer detection using A-train satellite lidar observations. *Geophys. Res. Lett.* **2015**, *42*, 620–628. [CrossRef]
44. Peng, L.; Snider, J.R.; Wang, Z. Ice crystal concentrations in wave clouds: Dependencies on temperature, D > 0.5 μm aerosol particle concentration, and duration of cloud processing. *Atmos. Chem. Phys.* **2015**, *15*, 6113–6125. [CrossRef]

45. Lauber, A.; Kiselev, A.; Pander, T.; Handmann, P.; Leisner, T. Secondary ice formation during freezing of levitated droplets. *J. Atmos. Sci.* **2018**, *75*, 2815–2826. [CrossRef]
46. Hallett, J.; Mossop, S.C. Production of secondary ice particles during the riming process. *Nature* **1974**, *249*, 26–28. [CrossRef]
47. Lawson, P.; Woods, S.; Morrison, H. The Microphysics of Ice and Precipitation Development in Tropical Cumulus Clouds. *J. Atmos. Sci.* **2015**, *72*, 2429–2445. [CrossRef]
48. Lawson, P.; Gurganus, C.; Woods, S.; Bruintjes, R. Aircraft Observations of Cumulus Microphysics Ranging from the Tropics to Midlatitudes: Implications for a "New" Secondary Ice Process. *J. Atmos. Sci.* **2017**, *74*, 2899–2920. [CrossRef]
49. Cesana, G.; Waliser, D.E.; Jiang, X.; Li, J.-L.F. Multimodel evaluation of cloud phase transition using satellite and reanalysis data. *J. Geophys. Res. Atmos.* **2015**, *120*, 7871–7892. [CrossRef]
50. Mülmenstädt, J.; Salzmann, M.; Kay, J.E.; Zelinka, M.D.; Ma, P.L.; Nam, C.; Kretzschmar, J.; Hörnig, S.; Quaas, J. An underestimated negative cloud feedback from cloud lifetime changes. *Nat. Clim. Chang.* **2021**, *11*, 508–513. [CrossRef]
51. Choi, Y.-S.; Lindzen, R.S.; Ho, C.-H.; Kim, J. Space observations of cold-cloud phase change. *Proc. Natl. Acad. Sci. USA* **2010**, *107*, 11211–11216. [CrossRef]
52. Korolev, A.V.; Isaac, G.A. Phase transformation of mixed-phase clouds. *Q. J. R. Meteorol. Soc.* **2003**, *129*, 19–38. [CrossRef]
53. Pinsky, M.; Khain, A.P. Some effects of cloud turbulence on water–ice and ice–ice collisions. *Atmos. Res.* **1998**, *47–48*, 69–86. [CrossRef]